Results in Physics 3 (2013) 7–13

Contents lists available at SciVerse ScienceDirect

Results in Physics

journal homepage: www.journals.elsevier.com/results-in-physics

Phase field modeling of Widmanstatten plate formation in Zr–2.5Nb material

G. Choudhuri [a], S. Chakraborty [b,*], D. Srivastava [c], G.K. Dey [c]

[a] Quality Assurance Division, Bhabha Atomic Research Centre, Mumbai 400085, India
[b] Radiometallurgy Division, Bhabha Atomic Research Centre, Mumbai 400085, India
[c] Material Science Division, Bhabha Atomic Research Centre, Mumbai 400085, India

ARTICLE INFO

Article history:
Received 29 June 2012
Accepted 21 December 2012
Available online 9 February 2013

Keywords:
Anisotropy
Parallel plate morphology
Phase field simulation
Diffuse interface
Zr–2.5Nb

ABSTRACT

Growth of Widmanstatten side-plates from pre-nucleated α in a matrix of β is a diffusion controlled process. The phase-field approach is formulated for Widmanstatten side plate formation through β-Zr (B.C.C) → α-Zr (HCP) transformation in binary substitutional Zr–2.5Nb alloy. Using Gibbs energy functional and diffusional mobility, microstructural evolution of parallel side-plates from pre-nucleated α phase has been simulated. The highly anisotropic nature of Widmanstatten plate and the presence of thin interface at the parent-product interface make the task challenging for FEM analysis. Based on this model, an estimate on the range of temperature over which Widmanstatten parallel side-plates can form is estimated and the extent of anisotropy of surface free energy on the morphology of the plates is analyzed.

1. Introduction

Zirconium alloys are widely used for fuel cladding, pressure tube and other core components in water cooled nuclear power reactors, *viz.*, Boiling Water Reactors (BWRs), Pressurized Water Reactors (PWRs) and Pressurized Heavy Water Reactors (PHWRs). The reasons for selecting Zirconium base alloys as a nuclear core materials are its low thermal neutron absorption cross-section, resistance to corrosion at high temperature aqueous environments, optimum mechanical properties and resistance to radiation damage. Alloying with Niobium improves its mechanical properties, corrosion properties and irradiation stability [1]. Zr–2.5Nb is one of the important alloy of Zr–Nb series. It is used as pressure tubes material in PHWRs. These pressure tubes are expected to serve for 30 years in reactor environment. The phase transformation and microstructural evolution in Zr–2.5Nb alloys are complex. Depending on soaking temperature and cooling rate, the β phase can be transformed into a variety of microstructures *viz.* allotriomorph alpha [2], Widmanstatten alpha with either parallel plates or basket weave morphology [3,4], martensitic microstructure [5–8], and omega phase [9]. Grain boundary allotriomorphs (GBA) nucleate and grow preferentially along the high angle grain boundaries of parent β phase. These are the first phase to form during β-Zr (Body Centre Cubic crystal structure) → α-Zr (Hexagonal Closed Packed structure) transformation with very low undercooling. With moderate or slightly higher undercooling Widmanstatten side plates form either by nucleating at grain boundaries or by branching out from GBAs. The β/α interface of the allotriomorphs which tend to propagate more toward the Burgers related β grains undergo a morphological instability [2] leading to the development of periodic protrusions. The broad faces of each protrusion have a very good atomic fit with parent lattice and due to difficulty in joining of individual atoms on the habit plane, thickening of the plates is restricted giving a very low value of mobility. These broad faces move forward by sideways motion of ledges and its tips grow linearly maintaining a constant radius of curvature.

The earliest model assuming a constant tip radius which would give maximum growth rate of a plate was given by Zener [10] and further modified by Hillert [11]. Livingston and Cahn [12] observed that the tip radius was larger than that expected to give the maximum growth rate. As a result the growth rate was, of course, less than the expected maximum velocity [13]. It has been reported [14] that the influence of the concentration field ahead of α/β interface is responsible for the growth of a group of α lath of identical orientation giving parallel plate morphology. Inter granular plates are the other variety of Widmanstatten microstructure resulting from random precipitation of alpha plates on a number of planes in one beta grain [14] due to the presence of randomly dispersed second phase particles in the matrix. The formation and growth

* Corresponding author. Tel.: +91 22 2559 6081; fax: +91 22 2550 5151.
E-mail address: gargi@barc.gov.in (S. Chakraborty).

2211-3797
http://dx.doi.org/10.1016/j.rinp.2012.12.003

Fig. 1. Typical Widmanstatten plates were found in Zr–2.5Nb alloy [6].

laths of different orientations in same region give rise to generation of basket weave morphology. With increasing cooling rate, or extent of super cooling, variation of packet size leads to significant changes in microstructure. Fig. 1 shows the typical Widmanstatten plates found during gas quenching from two phase region (α + β) in Zr–2.5Nb alloy. The primary α formed during holding in two phase region have planar interface.

Limited work [15,16] has been done in modeling of microstructural evolution in Zr–2.5Nb alloy during various thermo-mechanical processings. Development of desired microstructure with required texture in commercial Zr–2.5Nb alloy has been achieved through empirical formulation and traditional trial and error method which is expensive and very much time consuming. Hence, models that characterize microstructural features with anisotropy and texture are required to design the process route.

Over the last decade, phase-field method (PFM) [17–22] has emerged as a powerful computational tool for modeling and predicting the meso-scale morphological and microstructure evolution during solid–liquid and solid–solid phase transformations. In PFM explicit tracking of interface is not required. However, quantitative modeling at real length and time scales requires that the fundamental model inputs be linked to thermodynamic and mobility databases. Extensive work has been done by Chen and Wang [17,23] in developing and integrating thermodynamic modeling, mobility data base and phase field simulation to predict microstructural evolution in Ti base alloys mainly in Ti–6Al–4V alloy.

Two important aspects of the formation of the Widmanstatten morphology are the anisotropy in interfacial energy as well as anisotropy in attachment kinetics. In a phase field model, this anisotropy in attachment kinetics can be incorporated by making the mobility or relaxation parameters anisotropic.

In this paper, a phase-field model is presented for Zr–Nb substitutional system, which investigates the generation of parallel side plate morphology from pre-nucleated α utilizing Gibbs free energy and mobility functions. Anisotropy is introduced in the form of orientation-dependent grain-boundary energies. Based on this model, an estimate on the range of temperature over which Widmanstatten parallel side-plates can form is estimated and the extent of anisotropy of surface free energy on the morphology of the plates is analyzed.

2. Phase field model formulation

PFM is based on diffuse interface description developed by Vander Walls [24] and subsequently by Cahn and Hilliard [25] and Allen and Cahn [26]. The nature of the interface in PFM is different from the conventional approaches for microstructure modeling which takes mathematically sharp interface. PFM applies a continuum field, *i.e.* a phase field characterized by a set of conserved and non-conserved phase field variables. Conserved variables like concentration or mole fraction (c) satisfy the mass conservation condition. The non-conserved variables like order parameter (φ) contains information of local crystal structure or orientation of different domains. These order parameters in phase field models may or may not have macroscopic physical interpretations.

In the solid phase transformation, the non conservative continuously varying phase-field variable (φ) can be 0 in one phase and 1 in other phase. The spatial range over which φ changes from 0 to 1 is the width of the interface. This concept of a continuous non-conserved phase-field for distinguishing two coexisting phases was introduced by Langer [27]. The single-phase-field representation in combination with a composition field has been applied to study the growth of Widmanstatten side plate.

2.1. Free energy functional

Thermodynamic basis of model is depicted through free energy functional [32].

$$G = \int_v \left(\frac{g(\varphi, c, T)}{Vm} + \frac{\varepsilon_c^2}{2} |\nabla c|^2 + \frac{\varepsilon_\varphi^2}{2} |\nabla \varphi|^2 \right) dv \tag{1}$$

with $g(\varphi, c, T)$, the homogeneous free energy density at a given temperature (T K) is a function of phase field variables, *viz.,* order parameter φ (non conservative) and concentration c (conservative). Concentration (c) is expressed in terms of mole fraction of *Nb*. The molar volume (V_m) is assumed to be constant for both the phases and ε_φ and ε_c is the gradient energy coefficient for order parameter and concentration inhomogeneities respectively. Temperature (T K) is taken as constant due to rapid heat conduction.

This free energy density, $g(\varphi, c, T)$, associated with bcc to hcp phase transformation in Zr–Nb system can be constructed according to the symmetry changes from Landau free energy functional [28]. But getting a Landau free energy consistent with experimental equilibrium free energy data as well as the temperature and composition dependent parameters in the Landau free energy expansion is a tedious task.

Alternate approach, developed by Wang et al. [29], is using a phenomenological order parameter that considers different values for different phases. The local free energy is then obtained using the equilibrium free energy of individual phases. In this approach, the homogeneous free energy density consists of an interpolation function $fp(c, \varphi, T)$ and a double-well function $k(\varphi)$.

$$g(c, \varphi, T) = fp(c, \varphi, T) + k(\varphi) \tag{2}$$

The interpolation function fp combines the free energy expressions of the coexisting phases $G\alpha(c, \varphi, T)$ and $G\beta(c, \varphi, T)$ into one free energy expression, which is a function of the phase field variables c and φ, using a weight function $p(\varphi)$:

$$fp(c, \varphi, T) = (1 - p(\varphi))G\alpha(c, T) + p(\varphi)G\beta(c, T) \tag{3}$$

In this case φ is set to 0 in hexagonal closed packed (HCP) α phase and 1 in body centered cubic (BCC) β phase. c Is the mole fraction of *Nb*. The functions $G\alpha(c, T)$ and $G\beta(c, T)$ are homogeneous free energy expressions for the composition and temperature dependence of the α phase and the β phase. In our simulations these were taken from a paper titled "Thermodynamic analysis

of stable phases in Zr–Nb system and calculation of phase diagram" by Guillermet [30] and SGTE database for pure element by Dinsdale [31]. The complete expressions are given in Appendix A.

$p(\varphi)$ is a smooth function that equals 1 for $\varphi = 1$ and 0 for $\varphi = 0$ and has local extrema in between $\varphi = 0$ and $\varphi = 1$. Mostly, the following function [19].

$p(\varphi) = \varphi^3(10 - 15\varphi + 6\varphi^2)$ is used, for which $p'(\varphi) = 30q(\varphi)$.

The $k(\varphi)$ in Eq. (2) can be represented by

$$k(\varphi) = w * q(\varphi) = w * (\varphi^2 - 2\varphi^3 + \varphi^4) \tag{4}$$

where w is the kinetic barrier between the two minima in the double well free energy density representation and can be adjusted to fit the desired interfacial energy. And $q(\varphi) = (\varphi^2 - 2\varphi^3 + \varphi^4)$. At φ = 0 and 1 $q(\varphi)$ = 0 and it has maximum value at φ = 0.5.

The interface thickness is a balance between two opposing effects. The interface tends to be sharp in order to minimize the volume of material where φ is varying in between 0 and 1 and $q(\varphi)$ is large. While, the interface tends to diffuse to reduce the energy associated with the gradient of φ as described by ε_φ in Eq. (4). For pure material interface thickness (δ) is related with (ε_φ) and w by the expression, $\delta = \frac{\varepsilon_\varphi}{\sqrt{2w}}$ [19] and interfacial energy (σ) is related to them as $\sigma = \varepsilon_\varphi\sqrt{\frac{w}{18}}$ [19]. Combining the above two expressions, w becomes $\frac{3*\sigma}{\delta}$. For alloys apart from ε_φ, the thickness of diffuse interface also depends on the properties of phase diagram. Selzer et al. [32] showed that the thickness of interface in phase field solution remains almost unchanged with ε_φ when there is a large difference in equilibrium concentration of the phases. When the difference in equilibrium concentration of the phases is not significant, thickness of diffuse interface is directly related to ε_φ. In the present model, for simplification ε_φ and w were assumed as independent of temperature and composition and $\varepsilon_c = 0$. In case of spinodal decomposition $\varepsilon_c \neq 0$ but for isobar-thermal $\beta(b.c.c\ Zr) \rightarrow \alpha(h.c.p\ Zr)$ transformation ε_c can be assigned to zero as this will not affect the kinetics of Widmanstatten plate formation significantly.

2.2. Evolution equations

The evolution of non conserved and conserved phase field variables in a phase-field model can be obtained by solving the Allen–Cahn equation [26] and the Cahn–Hilliard diffusion equation taking the above mentioned total free energy (G) of the microstructure.

$$\dot{\varphi} = -M_\phi \frac{\delta G}{\delta \varphi} \tag{5}$$

$$\dot{c} = \nabla . L'' \nabla \left(\frac{\delta G}{\delta c}\right) \tag{6}$$

where $M\varphi$ is the order parameter mobility and can be directly related to interface mobility (M) in sharp interface approach as $M_\varphi = 0.0235M/\delta$ [33] which ensures diffusion controlled process and $L''$is related to the diffusional mobility of Nb atom (M_{Nb}) through $L'' = c(1-c)M_{Nb}$ [34]. As diffusivity of Nb in h.c.p and b.c.c phase is different [35–40], M_{Nb} can be represented by phase field parameter, $M_{Nb} = (M_{Nb}^{hcp})^{1-p(\varphi)} M_{Nb}^{bcc^{p(\varphi)}}$, where $M_{Nb}^{hcp} = \frac{D_{Nb}^{hcp}}{RT}$ and $M_{Nb}^{bcc} = \frac{D_{Nb}^{bcc}}{RT}$.

To get interfacial mobility, Turnbull's model [37] for the mobility of incoherent grain boundaries in a single phase material is considered. This model assumes that the atoms are transferred individually across the interface by a process related to diffusion and it yields the following type of relationship, $M = \frac{\delta_0 D_{eff} V_m}{b^2 RT}$, where δ_0 is the width of the incoherent boundary and b is the distance between atoms. D_{eff} is the effective diffusivity of the atoms in this process. In this case, it is taken as $D_{eff} = \left(D_{Nb}^{hcp^{0.5}} + D_{Nb}^{bcc^{0.5}}\right)^2$. D_{Nb}^{hcp} and D_{Nb}^{bcc} are the lattice diffusivity of α and β phase [36,40], respectively and are given in Table 1.

2.3. Anisotropy in interfacial energy and finite element method

Interfacial energy is the free energy associated with the compositional and/or structural in-homogeneities present at interfaces. Since in a phase-field method the interface is diffuse in nature, the proper incorporation of interfacial energy is of utmost importance. The extent of anisotropy in interfacial energy determines the morphology of the phase [13].

The β → α transformation in Zr based alloys follows the Burgers Orientation relation almost exactly, irrespective of whether the transformation is diffusional or martensitic [2], *i.e.*, $(0001)_{hcp}||(011)_{bcc}$, $(1-100)_{hcp}||(2-1-1)_{bcc}$ and $[11\text{–}20]_\alpha||[11\text{–}1]_\beta$. This orientation relationship results in a coherent or semi-coherent interface of very low energy. Alpha phase nucleated at beta phase grows along a specific crystallographic direction which depends on the relative orientation of the crystalline lattices of the two adjacent grains and also on the orientation of the phase interface. As β → α transformation in Zr based alloys follows the Burgers Orientation relation, it has been assumed that in the simulation thin beta and alpha plates are following the same orientation relationship.

In the case of Widmanstatten plates, the broad sides of the parallel plates are coherent in nature with minimum interfacial energy whereas the tip of the plate is incoherent in nature with the highest interfacial energy. This anisotropy in interfacial energy in solid state transformation can be introduced by using a function, $\eta = \eta(\theta)$ where $\theta = \arctan\left(\frac{\varphi_y}{\varphi_x}\right)$ which is nearly equal to the angle between interface normal and x axis. The thickness of the interface also varies due to anisotropy. Thickness of coherent interface is much smaller than incoherent interface. It has been proposed by McFadden et al. [41], that the diffuse interface thickness (δ) and the interfacial energy (σ) follow the same anisotropy. The relationship of interfacial energy and interface thickness with orientation can be written as follows.

$$\sigma = \sigma_0 * \eta(\theta); \quad \delta - \delta_0 * \eta(\theta);$$

where σ_0 and δ_0 are the maximum interfacial energy and maximum interface width which are the input parameters of the model, σ_0 = 0.3 J/m^2 (typical value for incoherent phase interfaces) and

Table 1
Simulation parameters for Phase Field Model.

Molar volume	V_m (m^3/mol)	1.4060e-5
Distance between atom	b (Å)	3.23
Incoherent interface thickness	δ_0 (nm)	5
Interfacial energy of incoherent interface	σ_0(J/m^2)	0.3
Nb diffusion coefficient in α-Zr	D_{Nb}^{hcp} (m^2/sec)	$6.6 * 10^{-10} * \exp(-15851.4/T)$
Nb diffusion coefficient β-Zr	D_{Nb}^{bcc} (m^2/sec)	$9 * 10^{-9} * (T/1136)\text{^}18.1 * \exp(-(25100 + 35.5 * (T-1136))/(1.98 * T))$

$\delta_0 = 5$ nm. Using the above relationships ε_φ becomes $\varepsilon_\varphi^2 = 6 * \sigma_0 * \delta_0 * \eta(\theta)^2$.

Anisotropy in interfacial energy and thickness is introduced by the following cosine function of θ, *i.e.*, $\frac{(1+\gamma|\cos(\theta-\theta_0)|)}{(1+\gamma)}$ [42] .Where θ_0 is the angle between the interfacial plane having good crystallographic fit and x axis. γ Is the extent of anisotropy. This function would give maximum interfacial energy (σ_0) when $\theta = \theta_0$ and minimum interfacial energy ($\sigma_0/(1+\gamma)$) when $\theta - \theta_0 = \pi/2$. So extent of γ controls the interfacial energy of coherent interface. To assure that Gibbs Thomson remains positive anisotropy function is regularized using a smooth function near $(\theta - \theta_0) = n * \pi/2$ as introduced by Loginova et al. [42].

For anisotropic interface

$$\frac{\delta G}{\delta \varphi} = -\varepsilon_\varphi^2 \nabla^2 \varphi + \frac{\partial}{\partial x}\left(\varepsilon\varepsilon'_\theta \frac{\partial \varphi}{\partial y}\right) - \frac{\partial}{\partial y}\left(\varepsilon\varepsilon'_\theta \frac{\partial \varphi}{\partial x}\right) + \frac{\partial g(\varphi, c, T)}{\partial \varphi} \tag{7}$$

And using

$$\frac{\partial g}{\partial \varphi} = p'(\varphi)\frac{G\beta - G\alpha}{V_m} + q'(\varphi)\frac{w}{V_m} \tag{8}$$

Thus the evolution Eq. (5) becomes

$$\frac{\partial \varphi}{\partial t} = M_\varphi\left[\varepsilon_\varphi^2 \nabla^2 \varphi - \frac{\partial}{\partial x}\left(\varepsilon\varepsilon'_\theta \frac{\partial \varphi}{\partial y}\right) + \frac{\partial}{\partial y}\left(\varepsilon\varepsilon'_\theta \frac{\partial \varphi}{\partial x}\right) + p'(\varphi)\frac{G\alpha - G\beta}{V_m} - q'(\varphi)\frac{w}{V_m}\right] \tag{9}$$

Similarly

$$\nabla \frac{\delta G}{\delta c} = \frac{\partial^2 g}{\partial c \partial \varphi}\nabla \varphi + \frac{\delta^2 g}{\delta^2 c}\nabla c \tag{10}$$

And using the expression of L'' and M_{Nb}, the evolution equation for conservative phase field variable becomes

$$\frac{\partial c}{\partial t} = \nabla.\left[c(1-c)\left(M_{Nb}^{hcp}\right)^{1-p(\varphi)}\left(M_{Nb}^{bcc}\right)^{p(\varphi)}\left(\frac{\partial^2 g}{\partial c \partial \varphi}\nabla \varphi + \frac{\delta^2 g}{\delta^2 c}\nabla c\right)\right] \tag{11}$$

For convenience Eqs. (9) and (11) were non dimensionalized using reference length $l = .9\delta_0$ and diffusion time $\tau = \frac{t * RT * M_{Nb}^{\alpha}}{l^2}$.

The other phase field parameters become $\widetilde{M}_\varphi = M_\varphi * \frac{l^2}{M_{Nb}^{\alpha} V_m}$, $\tilde{\varepsilon}_\phi = \frac{\varepsilon}{l * \sqrt{\frac{R*T}{V_m}}}$, $\tilde{\varepsilon}'_\theta = \frac{\varepsilon'_\theta}{l * \sqrt{\frac{R*T}{V_m}}}$ $\widetilde{G} = \frac{G}{RT}$, $\widetilde{w} = \frac{w}{RT}$, respectively. The dimensionless forms of the equations are given below.

$$\frac{\partial \varphi}{\partial \tau} = \widetilde{M}_\phi\left[\widetilde{\varepsilon}_\varphi^2 \widetilde{\nabla}^2 \varphi - \frac{\partial}{\partial \tilde{x}}\left(\widetilde{\varepsilon}\widetilde{\varepsilon}'_\theta \frac{\partial \varphi}{\partial \tilde{y}}\right) + \frac{\partial}{\partial \tilde{y}}\left(\widetilde{\varepsilon}\widetilde{\varepsilon}'_\theta \frac{\partial \varphi}{\partial \tilde{x}}\right)\right] + \widetilde{M}_\varphi\left[p'(\varphi)\frac{\widetilde{G}\alpha - \widetilde{G}\beta}{V_m} - q'(\varphi)\frac{\widetilde{w}}{V_m}\right] \tag{12}$$

$$\frac{\partial c}{\partial \tau} = \widetilde{\nabla}.\left[c(1-c)\left(\frac{M_{Nb}^{bcc}}{M_{Nb}^{\alpha}}\right)^{p(\varphi)}\left\{\frac{\partial^2 \tilde{g}}{\partial c^2}\widetilde{\nabla} c + \frac{\partial^2 \tilde{g}}{\partial c \partial \phi}\widetilde{\nabla}\varphi\right\}\right] \tag{13}$$

These two coupled PDEs are solved by finite element method using implicit time stepping and adaptive unstructured grid. The phase field equation shows very stiff gradient at the interface region and with realistic interface thickness of few nanometers the tasks of solving it becomes challenging. Due to requirement of huge computational power, we have taken incoherent interface thickness δ_0 as 5 nm and in non dimensional space the interface regions have been discretized using five grid points and the rest of the region with large triangles optimizing the computational load and accuracy of the solution. Zero flux Neuman boundary conditions were applied at the internal boundary.

3. Results and discussions

3.1. Phase-field simulations of growth of single protrusion of grain-boundary α

Phase-field simulations of growth of single protrusion of pre-nucleated α in β-Zr phase of Zr–2.5Nb alloy were performed at different temperatures. These temperatures were indicated in phase diagram of Zr–Nb (Fig. 2) [30]. The A and B specify the simulation temperatures for Widmanstatten plate formation and *C* for planar growth, respectively. Initial state was homogeneous β (with 0.025Nb) with a very thin layer of α having a *Nb* concentration of 0.007 (mole fraction). The initial protrusion of α on the planar surface had amplitude 6 l and length 15 l. In our simulations, we observed that Widmanstatten plate grows from the initial grain boundary protrusion of α, in Zr–2.5Nb alloy in the temperature range of 800–890 K when interfacial energy of coherent interface is 1/21th interfacial energy of incoherent interface, corresponding to $\gamma = 20$. Otherwise initial perturbation decays and the planar surface of grain-boundary allotriomorphs grows. So a higher value of γ is responsible for the growth of Widmanstatten plate in this temperature range. This is similar to the result obtained for the growth of grain boundary ferrite [42] in Fe–C system.

With an increase in γ from 20 to 120, the lengthening rate (increase of length per unit time) of the single Widmanstatten side plate (after omitting few initial steps) increases (Fig. 3) whereas

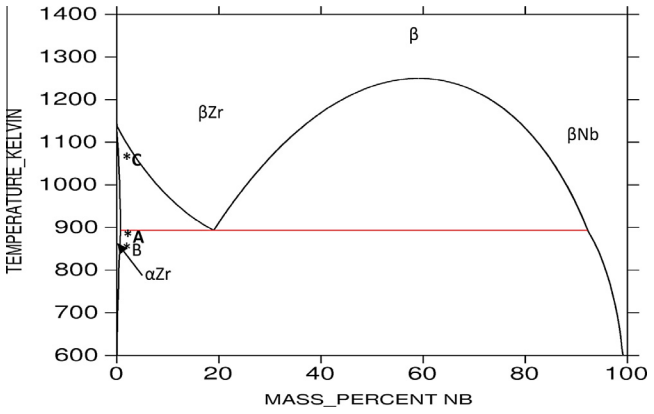

Fig. 2. Zr–Nb phase diagram. The points A and B specify the operating points for Widmanstatten plates and C for planar growth, respectively.

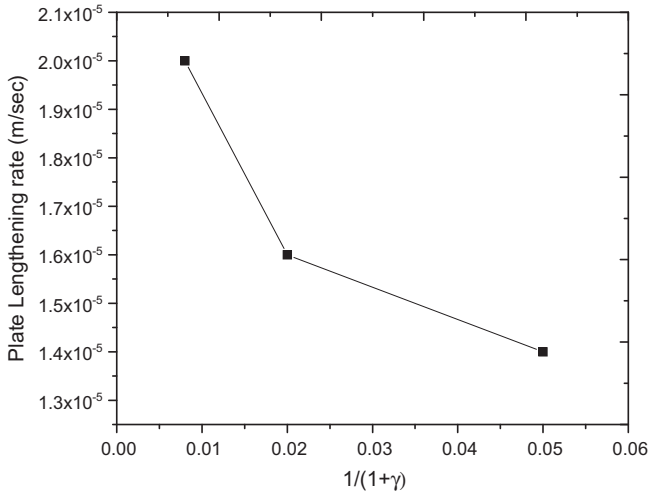

Fig. 3. Effect of γ parameter on the side plate lengthening rate.

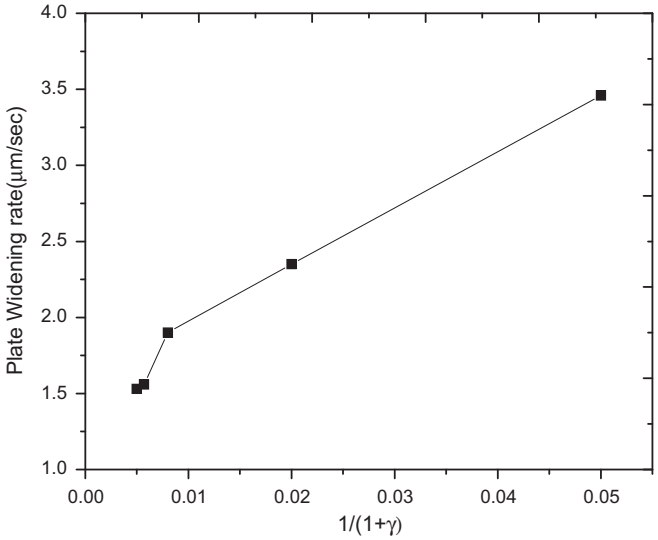

Fig. 4. Effect of γ parameter on the side plate widening rate.

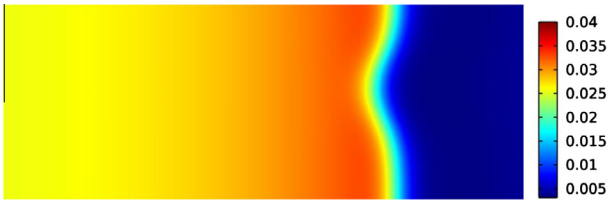

Fig. 5a. More or less uniform distribution of concentration field (mole fraction of *Nb*) across the entire interface leads to planar growth. The domain size is 3.88 × 1.5 μm.

the widening rate (increase in width per unit time measured after few initial steps) of the plate reduces (Fig. 4). With further rise in γ, no further change in widening rate is observed. Higher values of γ lead to the reduction of interfacial energy of two parallel coherent sides and lengthening of these two sides becomes more energetically favorable compared to widening of the plate and leads to the formation of plate with a high aspect ratio. To generate side plates with a high aspect ratio, a larger value of γ is required.

From an interfacial energy stand point, it is always favorable for a second phase precipitate to be surrounded by low energy coherent or semi coherent interfaces. If the crystal structure of the second phase is different from parent one, getting a common lattice plane is difficult. Nevertheless, there may be one plane that is identical in each crystal and with choosing correct orientation relationship a low energy coherent or semi coherent interface can form which must be bounded by high energy incoherent interfaces as usually no other plane of good matching present. From the γ plot of the interfacial energy, the Wulff theorem would predict the equilibrium shape to be a disk with a thickness/diameter ratio of γ_c/γ_i where γ_c and γ_i are the energies of the (semi) coherent and incoherent interfaces [43]. Deviation from equilibrium shape may be due to constraints imposed by the relative mobility of coherent/semi-coherent and incoherent interface as well as the presence of misfit strain energy effects. In phase field model, this aspect can also be incorporated by making the mobility or relaxation parameters anisotropic.

It was also observed from the model that the lengthening rate of single protrusion from grain boundary α depends on the relative velocity of tip with respect to the planar surface of pre-nucleated α. The movement of the planar surface of pre-nucleated α is restricted due to accumulation of solute atoms in front of it. The movement of the tip of Widmanstatten plate depends on how fast the excess solute atoms diffuse away from the tip. And it goes through a maximum as the radius of curvature increases. This is due to the fact that a smaller tip radius allows the excess solute atoms to diffuse away from the tip more rapidly and it also increases surface to volume ratio which leads to increase in requirement of energy in creating the surface. According to Zener, the plate would assume a radius consistent with maximum growth rate which is generally observed in practice. In the present model there is no need to specify the tip radius or the lengthening rate explicitly. The plate will attain a velocity due to interplay of different parameters like T(K), γ, σ and δ_0 (nm).

From the simulations, it was observed that the tip of the lath grows linearly after initial few steps. For $\gamma = 120$, $\delta_0 = 5$ nm, taking boundary as isoline of $\varphi = 0.5$ the tip velocity of Widmanstatten plate for Zr–2.5Nb alloy at 890 K is 20 μm/s. The width of the single lath grows slowly compared to tip and its growth rate in the initial stage is around 1.5 μm/s for the same γ. The single lath formed from pre-nucleated α can be divided into 3 regions, *viz.*, tip region, parallel sides and planar region. The tip region is incoherent characterized by the linear growth velocity. Parallel broad sides are coherent in nature. The velocity of these two parallel interfaces is parabolic in nature. The planar region of pre-nucleated α is incoherent in nature, although having parabolic velocity profile.

When simulations were performed at a higher temperature 1054 K (point C in Fig. 2) with γ greater than 20, the initial protrusion of grain boundary α does not grow into β to form a lath morphology, but it decays and the entire planar α grows and leads to the formation of allotriomorphs α. At higher temperatures due to higher diffusivity of solute atoms, solute pile up at the interface is less and rejected solutes from α phase build up more or less uniformly ahead of the entire interface including the tip region (Fig. 5a). The tip of the protrusion could not attain higher relative velocity with respect to the planar interface of pre-nucleated α and the protruded region decays and the growth of entire planar interface takes place. This is a classical diffusion controlled phase transformation. As temperature is lowered, movement of the planar surface of pre nucleated α is restricted due to accumulation of solute in front of it and the lower mobility of solute atoms helps in maintaining the difference in solute concentration at the tip and at the planar interface of pre nucleated α (Fig. 5b) and favored the growth of the single lath (point A in Fig. 2).

The distribution of non conservative phase field variable ϕ (Fig. 5c) deserved special attention. The large variation of interface width along the phase change boundary can be explained by the fact that interface thickness follows the same anisotropy function, as interfacial energy mentioned by McFadden et al. [41]. The two parallel sides of a single lath are coherent in nature whereas the tip is incoherent and the coherent interface is much thinner than incoherent interface. For perfect coherent interface, thickness is zero.

3.2. Phase-field simulations of multiple protrusions in grain boundary α

In the case of multiple side plates' formation from grain boundary α, interaction of diffusion field of neighboring protrusions changes the morphology of the growing phase. To simulate the formation of multiple plates from grain boundary α, protrusions of same size are generated at a particular distance in the domain of 3.5 × 1.5 μm.

The evolution of multiple side plates from grain boundary α with initial *Nb* concentration $c = 0.007$ was simulated at 890 K (point A in Fig. 2) using $\gamma = 120$. With increasing time it can be seen (Fig. 6) that the inter lath location becomes rich in solute content

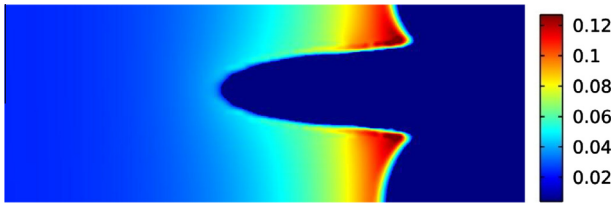

Fig. 5b. Distribution of concentration field (mole fraction of *Nb*) during lath formation. Movement of planar interface is restricted due to solute accumulation and growth of tip leads to lath formation. The domain size is 3.88 × 1.5 μm.

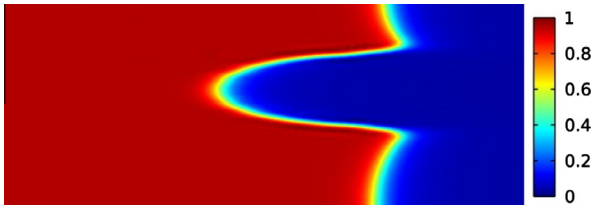

Fig. 5c. Distribution of phase field variable (ϕ) during lath formation. The domain size is 3.88 × 1.5 μm.

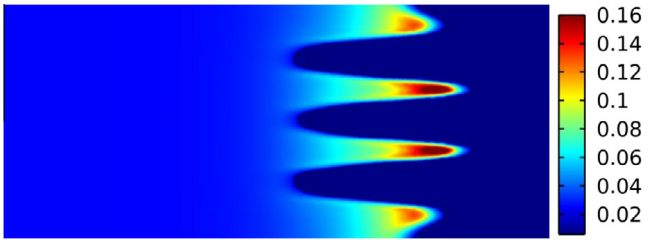

Fig. 6. Distribution of concentration field (mole fraction of Nb) during growth of multiple lath from allotriomorph α at 890 K. The domain size is 3.5 × 1.5 μm.

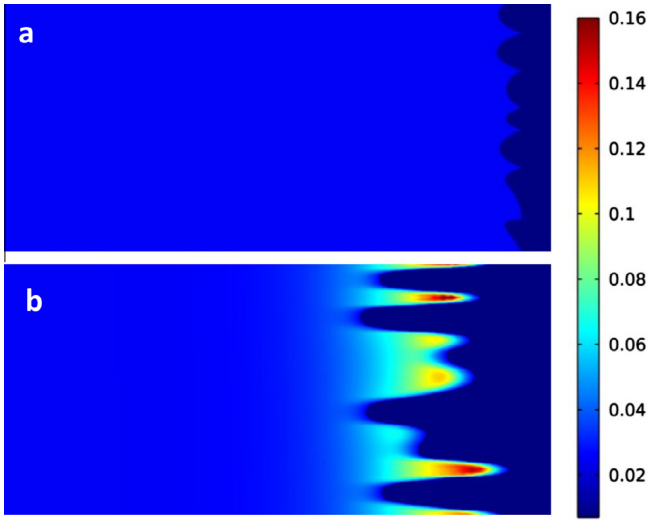

Fig. 7. (a) Distribution of concentration field (mole fraction of *Nb*) in initial microstructure having various sizes of protrusions of grain boundary α in a matrix of β. (b) Evolution of microstructure during growth of grain boundary α at 890 K. The domain size is 3.28 × 1.5 μm.

as the diffusion field of neighboring laths overlapped and prevents further widening of each lath. Depending on the position of the neighboring lath the width of each lath achieves a constant thickness which is lower than when the simulation is performed with a

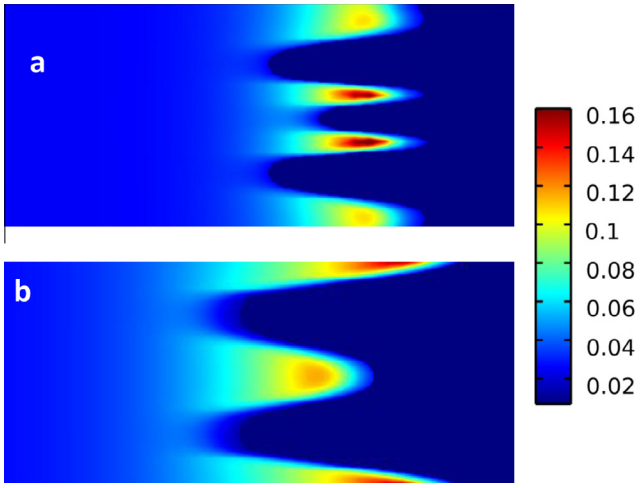

Fig. 8. Distribution of concentration field (mole fraction of *Nb*) during development of α phase of different morphologies from the initial protrusions of grain-boundary α, (a) lower temperature and (b) higher temperature lath morphology. The domain size is 2.4 × 1 μm.

Fig. 9. Distribution of concentration field (mole fraction of *Nb*) during development of allotriomorphs α from the protrusions of grain boundary α at 1054 K, The black line denotes the initial position of the interface. The domain size is 2.80 × 1 μm.

single lath. Further growth of the lath in width direction is restricted. When initial microstructure contains protrusions of various sizes (Fig. 7), it was observed that the initial protrusions which were wider grow faster than other ones. Certain protrusions do not grow at all due to interaction of diffusion field of neighboring ones.

Simulations were also performed with higher number density of protrusions in unit length of interface in a domain of 2.4 × 1 μm. It was observed that as temperature is lowered (870 K) (point B in Fig. 2), Widmanstatten plate width decreases. At lower temperatures, diffusion of excess solute atom from two broad surfaces of Widmanstatten plate becomes difficult and higher number of protrusions in unit length of interface are able to grow independently without overlapping of diffusion field, giving lath with lower thickness (Fig. 8a). At a higher temperature (890 K) if closely spaced protrusions are present, then due to overlapping of diffusion field of neighboring laths in front of the tip of in between protrusions, growth of in between protrusion may not take place at all leading to lesser number of coarser side plate (Fig. 8b). After a large number of simulations were performed at different temperatures with various sizes of initial perturbation, it was observed that a higher temperature leads to the formation of coarser lath irrespective of the position of neighboring protrusions. So the lath width is very much sensitive to the temperature of transformation.

Simulations were also performed at 1054 K (point C in Fig. 2) with a high value of γ (120). The starting microstructure consists of thin layer of domain of α with *Nb* content $c = 0.004$ in a matrix of β with *Nb* content $c = 0.025$. After simulations all the initial protrusions irrespective of their positions on grain boundary α, decay

and planar interface move in classical diffusion controlled process (Fig. 9).

4. Conclusions

The growth of Widmanstatten plates in Zr–2.5Nb alloy has been modeled taking thermodynamic and kinetic data of Zr–Nb system as an input. The effect of temperature and γ parameter during growth of single and multiple side plates has been evaluated. The lengthening rate of single α plate increases linearly with γ value whereas widening rate decreases. In case of multiple laths the phase fields of neighboring plates interact hindering the growth of plates in width direction resulting in different aspect ratios compared to a single lath. The side plates grow in a range of temperature. Higher temperature favors the formation of wider side plate. At very high temperatures with low undercooling, classical diffusional planar growth is observed rather than Widmanstatten growth. As the temperature is lowered, the movement of the planar surface is restricted and Widmanstatten growth is favored. The anisotropy in surface energy and the relative velocity of tip of the plate with respect to the planar surface of pre-nucleated grain-boundary α are responsible for the growth of Widmanstatten side plate. The variation of width of plates with variation of different thermomechanical processing parameters provides a scope for further study.

Acknowledgments

The authors are grateful to Shri S. Anantharaman, Head of Quality Assurance Division and Sri P.P Nanekar, Head of NDT Validation Centre, Quality Assurance Division for fruitful discussions and help during the preparation of the manuscript.

Appendix

Thermodynamic Description of Zr–Nb system [30,31]

$$^{\circ}G^{\beta}_{Zr} = -526.9 + +124.9457 * T - 25.607406 * T * \log(T) - 0.00034008415 * T^2 - 9.72897347 * .1 * 10^{-8} * T^3 - .761428942 * 10^{-10} * T^4 + \left(\frac{25233}{T}\right) \quad (14)$$

$$^{\circ}G^{\beta}_{Nb} = -8519.35 + 142.048 * T - 26.4711 * T * \log(T) - 0.000203475 * T^2 3.50119 * 0.0000001 * T^3 + \left(\frac{93398.8}{T}\right) \quad (15)$$

Interaction parameters in β phase,

$$L^{\beta}_0 = 15911 + 3.35 * T \quad (16)$$

$$L^{\beta}_{0i} = 3919 - 1.091 * T \quad (17)$$

$$iG^{\beta}_m = c *^{\circ} G^{\beta}_{Nb} + (1-c) *^{\circ} G^{\beta}_{Zr} + R * T * c * log(c) + R * T * (1-c) * log(1-c) + c * (1-c) * (L^{\beta}_0 + L^{\beta}_{0i} * (2 * c - 1)) \quad (18)$$

$$^{\circ}G^{\alpha}_{Zr} = -7829 + 125.649 * T - 24.1618 * T * \log(T) - 0.00437791 * T^2 - \left(\frac{34971}{T}\right) \quad (19)$$

$$^{\circ}G^{\alpha}_{Nb} = 1480.65 + 144.448 * T - 26.4711 * T * log(T) + 0.000203475 * T^2 - 3.50119 * 0.0000001 * T^3 + \left(\frac{93398.8}{T}\right) \quad (20)$$

Interaction parameter in α phase

$$L^{\alpha}_0 = 24411 \quad (21)$$

$$iG^{\alpha}_m = c *^{\circ} G^{\alpha}_{Nb} + (1-c) *^{\circ} G^{\alpha}_{Zr} + R * T * c * log(c) + R * T * (1-c) * log(1-c) + c * (1-c) * L^{\alpha}_0 \quad (22)$$

References

[1] Waterside corrosion of zirconium alloys in nuclear power plants, IAEA TECHDOC-996, p. 124–69.
[2] Banerjee S, Mukhopadhyay P. Diffusional transformation, phase transformations: examples from titanium and zirconium alloys, Pergamon Material Series, vol. 12. 2007.
[3] Holt RA. J Nucl Mater 1970;35:322.
[4] Perovic V, Weatherly GC, Fleck RG. Can Metall Q 1985;24:253–7.
[5] Chernyaeva TP et al. Probl At Sci Technol 2011(2):95–107.
[6] Saibaba N et al. J ASTM Int 2011;8(6).
[7] Banerjee S, Krishnan R. Acta Metall 1971;19:1317–26.
[8] Srivastava D et al. Mater Sci Eng 2000;A288:101–10.
[9] Tewari R et al. J Nucl Mater 2008;383(1–2):153–71.
[10] Zener C. TMS AIME 1946;167:550.
[11] Hillert M. Metall Trans 1975;6A:5–19.
[12] Livingstone JD, Cahn JW. Acta Metall 1974;22:495.
[13] Doherty RD. In: Cahn RW, Haasen P, editors. Physical metallurgy, vol. 2. 4th revised and enhanced ed. North Holland: Elsevier Science B.B.; 1996.
[14] Woo OT, Tangri K. J Nucl Mater 1979;79:82–94.
[15] Dunlop JWC et al. J Nucl Mater 2007;366:178–86.
[16] Massih AR, Jernkvist LO. Comput Mater Sci 2007;39:349–58.
[17] Chen LQ. Ann Rev Mater Sci 2002;32:113–40.
[18] Wheeler AA, Murray BT, Schaefer RJ. Phys D 1993;66D:243–62.
[19] Boettinger W et al. Ann Rev Mater Res 2002;32:163–94.
[20] Qin RS, Bhadeshia HKDH. Acta Mater 2009;57:2290–3382.
[21] Qin RS, Bhadeshia HKDH. Mater Sci Technol 2010;26(7).
[22] Wheeler AA, Boettinger WJ, McFadden GB. Phys Rev A 1992;45A:7424–40.
[23] Wang Y et al. JOM 2005:32–8.
[24] Van der Waals JD. Z Phys Chem 1894;13:657.
[25] Cahn JW, Hilliard JE. J Chem Phys 1958;28:258–67.
[26] Allen SM, Cahn JW. Acta Metall 1979;27:1085–95.
[27] Langer JS. In: Grinstein G, Mazenko G, editors. Directions in condensed matter physics, Singapore: World Scientific; 1986, p. 165–86.
[28] Provatas N, Elder K. Phase-field methods in material science and engineering.
[29] Wang SL et al. Physica D 1993;69:189.
[30] Guillermet AF. Z Metallkd 1991:478–87.
[31] Dinsdale AT. CALPHAD: Comput Coupling Phase Diagrams Thermochem 1991;15(4):317–425.
[32] Selzer M, Nestler B, Danilov D. Math Comput Simul 2010;80:1428–37.
[33] Loginova I, Odqvist J, Amberg G, Ågren J. Acta Mater 2003;51:1327–39.
[34] Singer HM et al. Acta Mater 2009;57:116–24.
[35] Tiwari GP, Sharma BD, Raghunathan VS, Patil RV. J Nucl Mater 1973;46:35–40.
[36] Dyment F, Libanati CM. J Mater Sci 1968;3:349–59.
[37] Turnbull D. Trans AIME 1951;191:661.
[38] Piotrkowski R, Dyment F. J Nucl Mater 1986;137:94–9.
[39] Piotrkowski R. J Nucl Mater 1991;183:221–5.
[40] Federer JI, Lundy TS. Trans Met Soc AIME 1963;227:592.
[41] McFadden GB, Wheeler AA, Braun RJ, Coriell SR. Phy Rev E 1993;48:3.
[42] Loginova I, Ågren J, Amberg G. Acta Mater 2004;52(13):4055–63.
[43] Porter DA, Easterling KE, Phase transformation in metal and alloys, 2nd ed. Chapan & Hall; 1996.